Kovove Mater. 63 2025 181–194 DOI: <u>10.31577/km.2025.3.181</u>

Friction and wear behavior of AlSi10Mg-TiB₂ composites with graphene nanoplatelets as a solid lubricant prepared using spark plasma sintering

Viktor Puchý^{1*}, Richard Sedlák¹, Róbert Džunda¹, Karol Kovaľ¹, František Kromka¹, Mária Podobová¹, Lucia Čiripová¹, Michal Besterci¹

¹Institute of Materials Research, SAS, Watsonova 47, 040 01 Košice, Slovak Republic

Received 14 July 2025, received in revised form 11 September 2025, accepted 7 Ocrober 2025

Abstract

The research focuses on the preparation, microstructure, and tribological properties of AlSi10Mg composites, reinforced with 10 wt.% TiB₂ particles and 2 wt.% graphene nanoplatelets (GNPs). The composites were prepared using the "Spark Plasma Sintering" (SPS) method to achieve high density and maintain the integrity of the added phases. Microstructural analysis confirmed the successful incorporation of TiB₂ and GNPs into the aluminum matrix. The addition of TiB₂ led to an increase in hardness and wear resistance. The addition of GNPs resulted in a further increase in hardness, a decrease in wear rate, and a significant reduction in the friction coefficient. Surface analysis revealed that the GNPs create a continuous and stable friction layer on the contact surface during the sliding test. This layer effectively prevents direct metal-to-metal contact, thereby changing the dominant wear mechanism from abrasive and adhesive to delamination, which reduces friction losses.

 $K\,e\,y$ w o r d s: aluminum matrix composites, $TiB_2,$ graphene nanoplatelets, spark plasma sintering, wear

1. Introduction

The increasing demand for reducing energy consumption and extending the service life of mechanical systems in the automotive, aerospace, and manufacturing industries is driving the development of new lightweight materials with excellent mechanical and tribological properties [1]. Aluminum Matrix Composites (AMCs) are particularly promising in this regard due to their low density, high specific strength, good thermal conductivity, and the ability to tailor properties by adding reinforcing phases [2]. The AlSi10Mg alloy is one of the most widely used matrices for AMCs due to its excellent castability, weldability, and favorable response to heat treatment, and is also widely used in additive manufacturing [3]. However, it does not have sufficient wear resistance on its own for many demanding applications. To improve wear resistance, hard ceramic particles such as SiC, Al₂O₃, or TiB₂ are commonly added to aluminum alloys. Titanium

diboride (TiB₂) is considered a particularly suitable reinforcement due to its extreme hardness, high elastic modulus, thermodynamic stability, and good wetting by molten aluminum [4]. Many studies have confirmed that the addition of TiB₂ particles effectively increases the hardness and abrasion resistance of aluminum composites by allowing the hard particles to carry the load and protect the matrix [5]. However, the presence of these hard particles often leads to a high coefficient of friction (COF) and can cause severe abrasive damage to the opposing sliding body. To address this problem, the concept of self-lubricating materials, where a solid lubricant phase is added in addition to the hard reinforcement, is emerging. Graphene nanoplatelets (GNPs) have proven to be an ideal candidate due to their unique two-dimensional structure in which atoms are arranged in a single or few atomic layers with strong in-plane bonds but weak out-of-plane interactions, which allows easy sliding between layers, excellent mechanical strength, and high thermal conductiv-

^{*}Corresponding author: e-mail address: vpuchy@saske.sk

ity that helps to remove heat from the contact zones [6]. The addition of GNPs to metal matrices can dramatically reduce the friction coefficient and wear rate by forming a protective and self-lubricating friction layer (tribolayer) on the worn surface [7]. The combination of hard ceramic particles and a two-dimensional material that reduces friction and wear by providing an easy shear plane between sliding surfaces in a single matrix leads to the creation of so-called hybrid composites, which can synergistically combine the advantages of both types of reinforcement: high wear resistance and low friction [8]. However, the manufacturing process is crucial for the success of such materials. Spark Plasma Sintering (SPS) is an advanced powder metallurgy technique that utilizes pulsed direct current and uniaxial pressure to consolidate powders rapidly. Short sintering times and lower temperatures compared to conventional methods enable the production of materials with high density and a fine microstructure, while minimizing unwanted chemical reactions at the matrix-reinforcement interface. This is particularly important for preserving the structure and functionality of graphene [9]. Although studies focusing on Al-TiB₂ or Al-GNPs composites exist, systematic research on the AlSi10Mg-TiB₂-GNPs hybrid system prepared by SPS and a detailed analysis of its tribological mechanisms are still limited [10]. Therefore, this work aims to prepare the AlSi10Mg-10TiB₂--2GNPs hybrid composite by the SPS method, systematically investigate the effect of GNPs addition on the microstructure, hardness, and tribological properties (friction and wear), and clarify the wear mechanisms with emphasis on analyzing the formation and function of the self-lubricating graphene friction layer on worn surfaces.

2. Materials and methods

The AlSi10Mg powder raw alloy, with particle sizes ranging from 20 to 56 µm, was supplied by ECKA Granules Germany GmbH (Velden, BY, Germany), and it contained 10 wt.% TiB₂ (2-6 µm powder with a purity of 99 %, Höganäs) has been used as the base material. The above powders were mixed with the addition of 2 wt.% of GNPs (graphene nanoplatelets aggregates with a specific surface area $500 \,\mathrm{m}^2 \,\mathrm{g}^{-1}$, submicron particles powder, Alfa Aesar). The mixing process was performed using a three-dimensional mixing device, "Turbula". All powders were milled with a rotation speed of 50 rpm for 2 h. Finally, the mixtures were sintered using Spark Plasma Sintering (SPS) (HP D 10SD, FCT Systeme, Frankenblick, Germany) at a temperature of 500 °C for 10 minutes with an uniaxial pressure of 50 MPa (16 kN). The sintered compacts were disc-shaped, measuring 20 mm in diameter and approximately 4 mm in height. The sample surfaces

were then ground and mechanically polished. The densities of the sintered samples were measured by the Archimedes hydrostatic weighing method. The hardness was determined by the Vickers method. The XRD measurements were performed on a laboratory X-ray diffractometer (Philips X'Pert Pro) using the Bragg-Brentano geometry. A Co X-ray source was employed, with wavelengths $K_{\alpha_1} = 0.178897 \,\mathrm{nm}$ and $K_{\alpha_2} =$ 0.179285 nm, and an intensity ratio of $K_{\alpha_1}/K_{\alpha_2}=0.5$. Data were collected with a step size of 0.033° and a counting time of 30 s per step. The local microstructures were analyzed using a Scanning Electron Microscope (SEM) (JEOL JSM-7000F, Nieuw-Vennep, The Netherlands) in backscattered electron (BSE) mode. Tribological tests were conducted on an automatic tribometer (HTT CSM Instruments, Switzerland) under rotational dry sliding conditions, employing a ballon-disc configuration at room temperature and atmospheric pressure. A 6 mm diameter ZrO₂ ceramic ball and a 100Cr6 steel ball were used as the friction counterpart. All tests were performed with a 0.25 and 0.5 N normal load, a sliding velocity of $0.1 \,\mathrm{m \, s^{-1}}$, and a total sliding distance of 100 m.

3. Results and discussion

3.1. Sintering regimes

The graphs in Fig. 1 show process parameters during SPS for three different material systems: pure AlSi10Mg, AlSi10Mg-TiB₂ composite, and AlSi10Mg-TiB₂-GNPs hybrid composite. The axes show the values of sintering temperature (°C), piston movement (mm), and force (kN) as a function of time (s). From an initial temperature of 400°C, a rapid increase in temperature occurs after approximately 450 s, with the maximum temperature reaching approximately 530°C during the sintering of the AlSi10Mg allov (Fig. 1a). This temperature is subsequently stabilized and maintained at 500°C for 600 s. Significant densification occurs in parallel with the increase in temperature. The maximum value of movement is 4.4 mm. The pressing force reaches a value of 16 kN, which remains stable during the holding period at the sintering temperature. The temperature profile during sintering of the AlSi10Mg-TiB₂ composite (Fig. 1b) is very similar to that of the pure matrix; the maximum temperature is also ~ 530 °C. The piston moves to a lower maximum value ($\sim 4.2 \, \text{mm}$), indicating an increase in the material's stiffness due to the addition of TiB₂. The maximum force again reaches 16 kN. An identical temperature profile is repeated during the sintering of the AlSi10Mg-TiB₂-GNPs composite (Fig. 1c), but a slightly lower maximum temperature is achieved $(\sim 525\,^{\circ}\text{C})$. A significantly lower maximum value of movement (~ 3.6 mm) is also achieved, indicating even

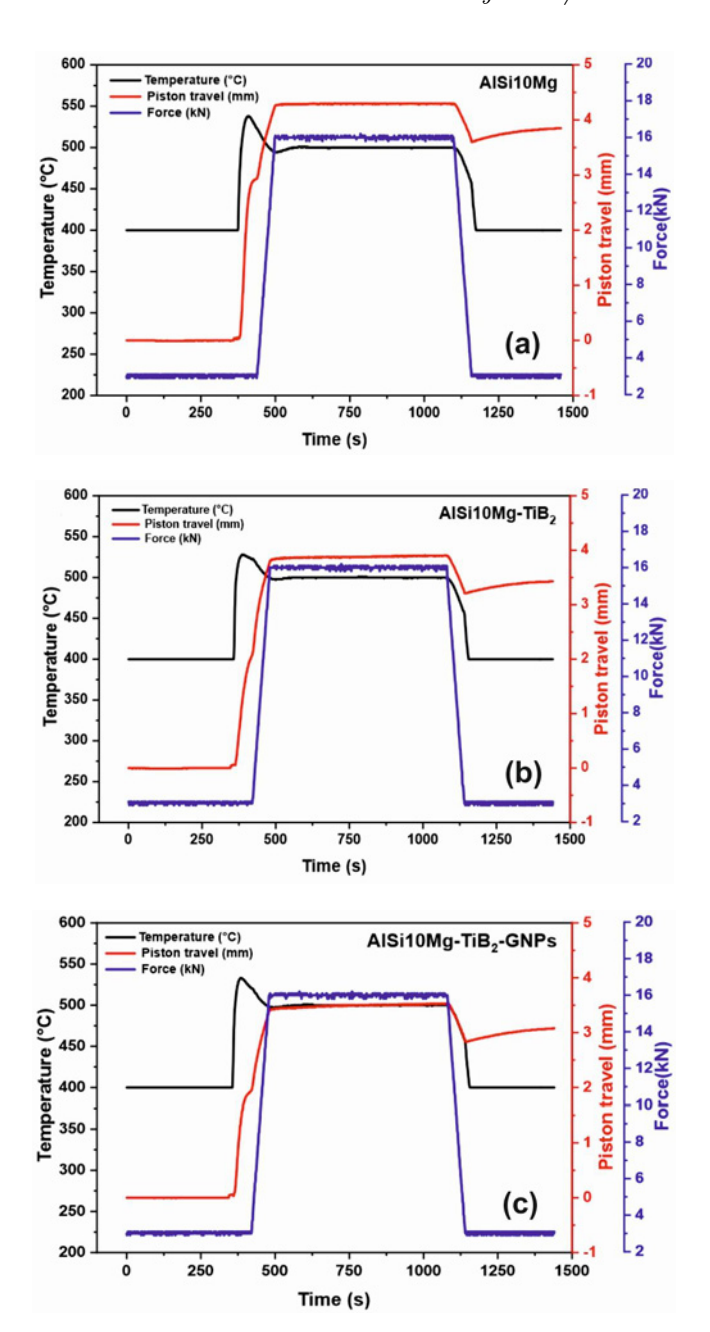


Fig. 1. SPS cycle, piston displacement with temperature and pressure over time.

higher stiffness and more effective compaction in the earlier stages of sintering. The maximum pressing force is again $16\,\mathrm{kN}$. The addition of TiB_2 leads to an increase in mechanical resistance during sintering, which is reflected in reduced piston movement. The combination of TiB_2 and GNPs further reduces the piston displacement, indicating a synergistic effect of both reinforcements on the compaction and mechanical strength of the composite. Therefore, it can be concluded from the sintering curves that the additions of ceramic reinforcements (TiB_2) and hybrid reinforcements (TiB_2) significantly af-

fect the compaction process during the SPS process. There is a reduction in plastic deformation during sintering, indicating higher stiffness and potentially better mechanical properties of the resulting composite. A similar reduction in piston displacement was observed in a study by Rashad et al. [11] when graphene nanoplatelets (GNPs) were added to the aluminum matrix sintered by the SPS method. Graphene prevented the deformation of aluminum particles and supported the slip mechanisms at the grain boundaries. Additionally, GNPs, as a two-dimensional nanomaterial, can serve as reinforcement in composites, further reducing diffusion distances and improving heat flow, thereby optimizing the development of the microstructure.

3.2. Density

The measured relative density values indicate a high compactness of the AlSi10Mg sintered material, with a value of 98.7 % indicating almost complete densification during the SPS process. The addition of 10 wt.% TiB₂ led to a decrease in the relative density to 93.7%, which can be attributed to the presence of hard ceramic particles, reducing the metal matrix's ability to achieve complete sintering due to poorer diffusion and lower plasticity of the system. The introduction of another 2 wt.% GNPs into the AlSi10Mg-TiB₂ composite causes a further decrease in relative density, indicating more pronounced barrier effects against densification. This phenomenon may be related to the tendency of GNPs to agglomerate, increased volume of the interfacial interface, and possible disruption of transport mechanisms during sintering. Overall, the results indicate that although ceramic and carbon additives improve some functional properties of composites, in terms of density, they reduce the efficiency of the SPS process compared to the pure alloy.

$3.3.\ Microstructure$

The results of the XRD studies are detailed in Fig. 2. The diffraction patterns revealed the presence of aluminum with a cubic lattice (space group Fm-3m) and a lattice parameter of $a=0.405\,\mathrm{nm}$, as well as silicon with a cubic lattice (space group Fd-3m:1) and a lattice parameter of $a=0.543\,\mathrm{nm}$ in all samples. In the AlSi10Mg-TiB2 and AlSi10Mg-TiB2-GNPs composites, TiB2 was also detected, exhibiting a hexagonal lattice (space group P6/mmm) with lattice parameters $a=0.303\,\mathrm{nm}$ and $c=0.323\,\mathrm{nm}$. No graphene was detected in any of the samples.

The microstructure images in Fig. 3 were obtained using SEM in backscattered electron (BSE) mode, which enables compositional contrast to be displayed. Figure 3a shows the microstructure of the AlSi10Mg

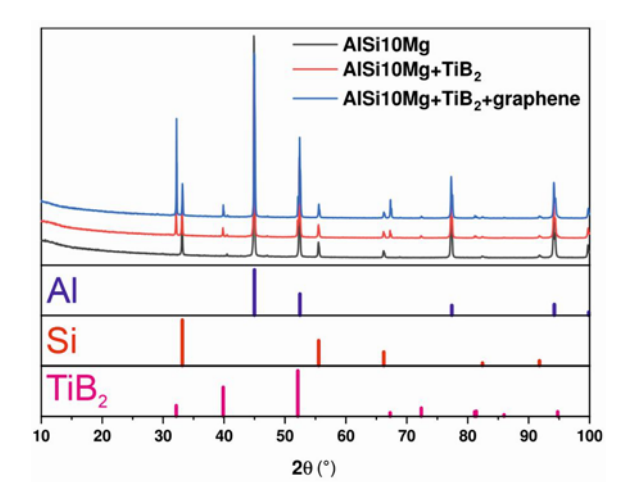


Fig. 2. X-ray diffraction spectra of sintered samples.

alloy prepared by SPS. The microstructure is composed of several distinguishable phases. The dominant phase is the matrix formed by an aluminum-based solid solution (α -Al), which is represented by extensive light gray areas. These areas are formed by the original, sinter-bonded powder particles that have re-

tained their approximately equiaxial shape. A fine, almost continuous network defines the boundaries of the original powder particles. This network is formed by the aluminum-silicon (Al-Si) eutectic that was formed during solidification or sintering in the intergranular regions. Due to the fine morphology, this network appears as darker lines and areas bordering the light gray matrix grains. Fine, light particles are dispersed within the α -Al matrix, as well as in the eutectic network. Given the composition of the alloy, these are precipitates of almost pure silicon (Si). Silicon has a higher atomic number than aluminum, and therefore appears as a lighter phase in the compositional contrast. These particles typically have an irregular to globular shape. Dark to black areas of irregular shape are also visible in the structure. These areas represent pores, which are a characteristic feature of sintered materials. They arise as a result of incomplete compaction of the metal powder during the pressing and sintering processes. The overall morphology suggests a structure formed by the joining and partial remelting of the original powder particles, which is consistent with the microstructures of AlSi10Mg alloys prepared by additive manufacturing or powder metallurgy methods, where a fine eutectic network is

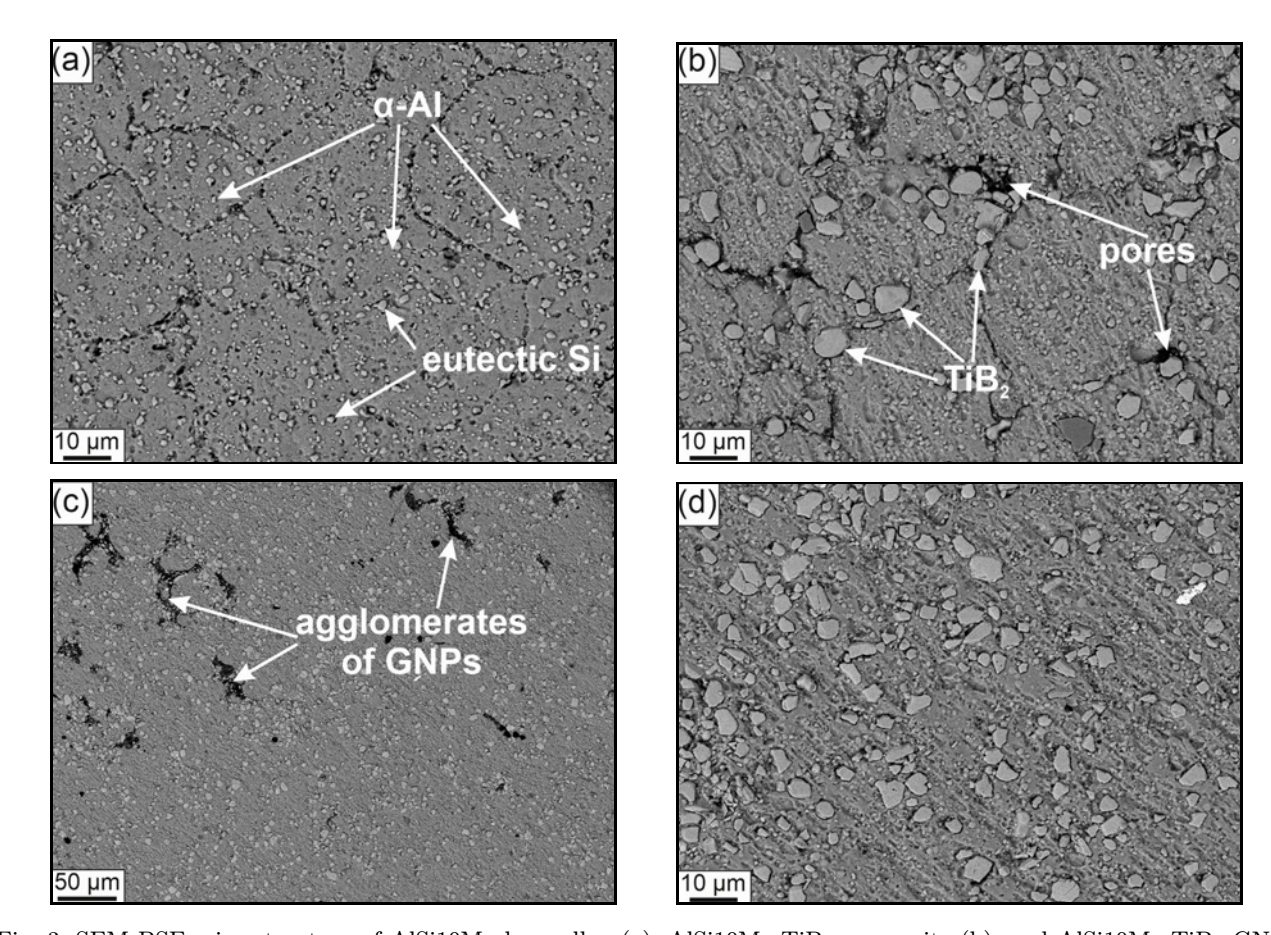


Fig. 3. SEM BSE microstructure of AlSi10Mg base alloy (a), AlSi10Mg-TiB₂ composite (b), and AlSi10Mg-TiB₂-GNPs composite (c),(d).

formed at the boundaries of the original powder particles [13].

Figure 3b shows a composite material with a metal matrix formed by an AlSi10Mg alloy, which is reinforced by the addition of 10 wt.% TiB₂ ceramic particles. Similar to the previous case, the microstructure is based on an AlSi10Mg alloy matrix, which appears as a continuous gray phase. This matrix is formed by the original metal powder particles that are bonded together. The most marked elements in the microstructure are light, almost white TiB₂ particles of irregular, sharp-edged to partially rounded shape. Their high brightness in the BSE mode is due to the presence of titanium, which has a significantly higher atomic number compared to aluminum and silicon. The TiB₂ particles are distributed mainly in the intergranular regions, i.e., at the boundaries of the original AlSi10Mg powder particles. This phenomenon, where ceramic particles are extruded to the matrix grain boundaries during sintering, is a typical mechanism in composites prepared by powder metallurgy and has also been observed in Al-TiB₂ systems [14]. The matrix grain boundaries are formed by a complex mixture. There is both a fine Al-Si eutectic (similar to that in the unreinforced material), but above all, the aforementioned massive TiB₂ particles are incorporated here. The eutectic network is significantly disrupted and discontinuous due to the presence of large ceramic particles. Dark to black areas in the structure indicate the presence of pores. Pores are often located near the matrix-ceramic particle interface, which may be caused by insufficient wetting of the ceramic by the molten phase during sintering or by different thermal expansions of both materials. Some dark areas may also represent cavities from TiB2 particles that were torn from the surface during polishing. A hybrid composite material is shown in Figs. 3c and 3d. The matrix is made of AlSi10Mg alloy and is reinforced by a combination of $10 \text{ wt.} \% \text{ TiB}_2$ particles and 2 wt.% GNPs. The gray background of the structure is made of the AlSi10Mg alloy matrix. Bright, white particles with sharp-edged to rounded morphology are clearly visible in the structure. These are TiB₂ particles. They are distributed relatively evenly, mainly at the grain boundaries of the matrix, where they settled during the sintering process. The key difference compared to the previous samples is the presence of GNPs. Due to the very low atomic number of carbon, which forms GNPs, this phase appears as a dark gray to black color. In the image, GNPs are primarily observable as agglomerates (clusters). The largest such agglomerate is located in the left part of the image and has an irregular, flaky appearance. The formation of such clusters is a well-known and common problem in the production of graphene-reinforced composites, as Van der Waals forces and the high surface area ratio of graphene lead to its agglomeration at the matrix grain boundaries [15]. These dark areas resemble pores in contrast, but are distinguished by their textured and less defined shape. There are also black areas in the structure, which represent pores – cavities formed during the compaction process. It is important to note that the presence of GNP agglomerates can contribute to increased porosity, as these clusters prevent perfect metallurgical bonding of the matrix particles. The matrix grain boundaries are the most complex part of this hybrid composite. They are formed by a mixture of Al-Si eutectic, massive ${\rm TiB}_2$ particles, and agglomerates of GNPs.

3.4. Mechanical properties

The Vickers hardness values of the composites were measured on a polished surface in the center of the sample. The influence of the different phases is clearly observable in the hardness values. The pure AlSi10Mg alloy has a hardness of $59.5\pm1.4~\rm HV1$. The AlSi10Mg-TiB $_2$ composite sample has a higher hardness than the pure AlSi10Mg sample. Similarly, the AlSi10Mg-TiB $_2$ -GNPs composite has a higher hardness than the AlSi10Mg-TiB $_2$ composite. This behavior is attributed to the achievement of the ceramic phase matrix, as TiB $_2$ has higher hardness than the matrix. The addition of another phase – GNPs – to the composite resulted in a final hardness of $65.8\pm2.5~\rm HV1$. The hardness of the AlSi10Mg-TiB $_2$ composite sample was at the level of $60.3\pm1.5~\rm HV1$.

3.5. Tribological results

Figure 4 shows the surface topography of the materials after tribological tests with a ZrO₂ ceramic ball (Figs. 4a,c,e) and a 100Cr6 steel ball (Figs. 4b,d,f), at a load of 0.25 N and a total friction path of 100 m. The surface of pure AlSi10Mg (Figs. 4a,b) shows a pronounced tribological track, characterized by a large depth and significant defects with a maximum height difference of up to approximately 36.5 µm. The track is deep and significantly uneven, indicating intensive material wear, abrasive damage, and potential material peeling in the central part of the track. The presence of TiB₂ in the AlSi10Mg matrix (Figs 4c,d) significantly reduces the depth and intensity of wear. The maximum height differences reach approximately 19.2 μm. The surface track is shallower, more uniform, and shows lower overall abrasion damage, indicating better resistance to tribological wear compared to pure AlSi10Mg. The material doped with GNPs and TiB₂ particles (Figs. 4e,f) has a tribological track with the lowest damage depth (approximately 19 µm). The surface is significantly uniform and smooth, with minimal defects and low wear. This phenomenon indicates the synergistic action of GNPs and TiB₂ in the composite, resulting in optimal tribo-

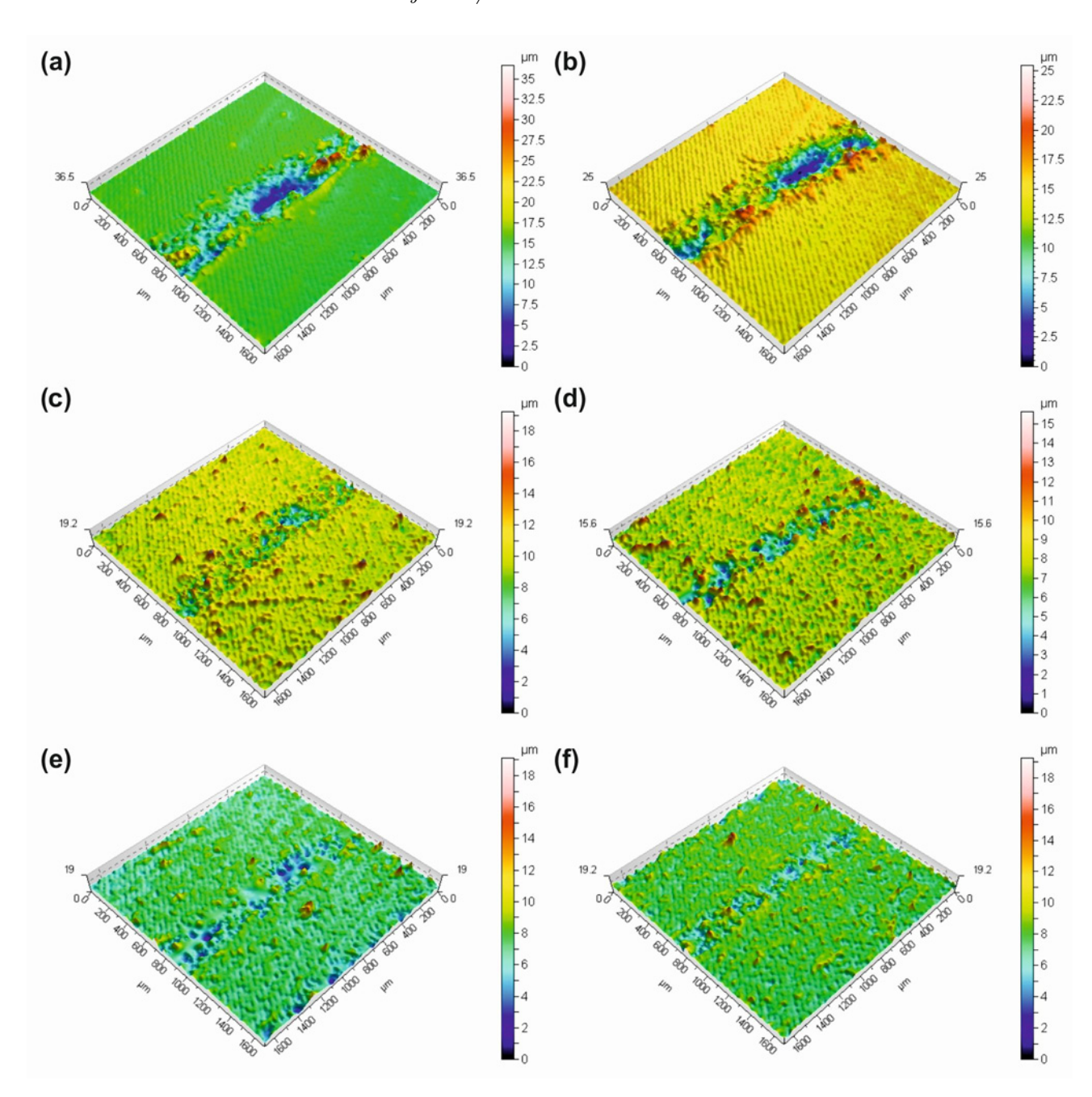


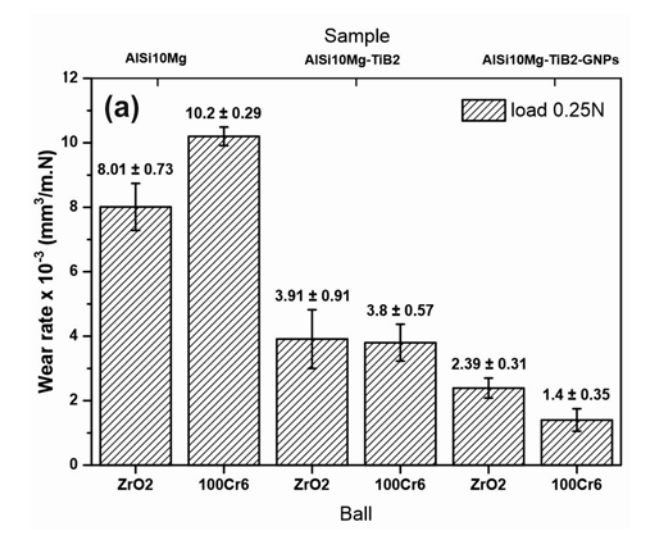
Fig. 4. Axonometric view of the topography of the friction paths of materials against ZrO₂ ceramic ball (a), (c), (e) and 100Cr6 steel ball (b), (d), (f) at a load of 0.25 N.

logical properties. By comparing the materials, it was found that the pure AlSi10Mg alloy exhibits the lowest resistance, significant non-uniformity, and abrasive damage. In contrast, the AlSi10Mg-TiB₂ composite shows improved homogeneity and increased resistance to tribological wear. Furthermore, the AlSi10Mg-TiB₂-GNPs composite demonstrates the best resistance, a homogeneous surface, and minimal damage.

3.6. Wear rate

Figure 5 shows the wear rate values of the inves-

tigated materials. The addition of TiB₂ reduces the wear rate at 0.25 N to approximately 1/2–1/3 of the pure alloy value and at 0.5 N to $\sim 60\,\%$ (ZrO₂) to $\sim 40\,\%$ (100Cr6) of the original value (Fig. 5b). The synergy of TiB₂ + GNPs brings the lowest wear rate of all investigated systems, at 0.25 N it achieves a reduction of 70–86 % compared to AlSi10Mg and 39–63 % compared to the composite with TiB₂. The comparison with a load of 0.5 N confirms the lubricating effect of GNPs against ZrO₂ ceramic ball (decrease to 1.78×10^{-3}), but against 100Cr6 steel ball, it increases to 3.62×10^{-3} , but still remains $\sim 70\,\%$ below



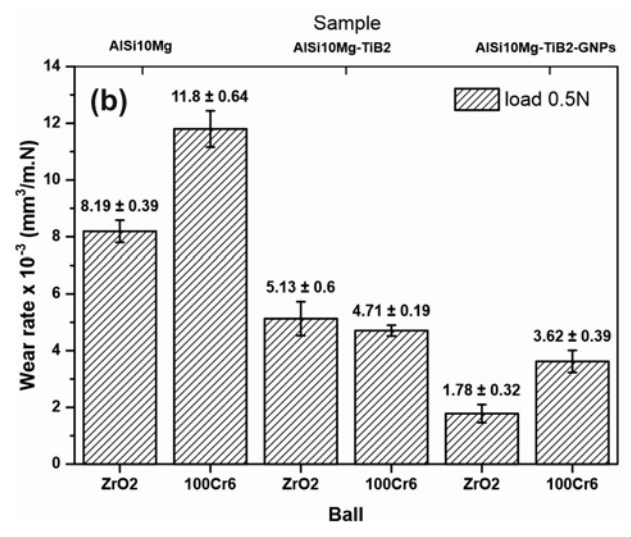


Fig. 5. Wear rate graph of AlSi10Mg, AlSi10Mg-TiB₂, and AlSi10Mg-TiB₂-GNPs composite at rotational speed of 0.1 m s⁻¹, length of 100 m, and friction force of 0.25 N (a) and 0.5 N (b).

the level of AlSi10Mg. The pure alloy shows virtually no sensitivity to load change in the pair with $\rm ZrO_2$ ceramic ball (8.01 \rightarrow 8.19 \times 10⁻³), while in contact with 100Cr6 steel ball increases by \sim 15 %.

The composite with TiB_2 behaves in the opposite way: increasing the pressure increases the wear rate with a ZrO_2 ceramic ball by ~ 31 %, but against a 100Cr6 steel ball, only by ~ 24 %. The composite with TiB_2 -GNPs shows a paradoxical phenomenon. With a ZrO_2 ceramic ball, the load increases the wear rate by only ~ 25 %, while with a 100Cr6 steel ball, it increases by 2.6 times; i.e., the graphene film is more easily damaged on steel than on ceramics at higher loads. For both AlSi10Mg and the composite with TiB_2 , the steel counterpart results in wear that is ~ 25 –45 % higher compared to the ZrO_2 ce-

ramic. On the contrary, the graphene composite exhibits a lower wear rate against steel at 0.25 N; however, at 0.5 N, the trend reverses, indicating the sensitivity of the graphene tribofilm to local contact pressure. TiB₂ ceramic particles significantly strengthen the AlSi10Mg matrix. At a low load of 0.25 N, the wear rate is reduced by at least 50 % regardless of the ball type. The addition of GNPs brings the greatest benefit at lower loads, dropping to values of 1.4- $2.4 \times 10^{-3} \,\mathrm{mm^3 \, N^{-1} \, m^{-1}}$, which represents a record decrease of 70-86% compared to the base alloy. ZrO_2 acts as a more favorable counterpart for both pure and TiB₂-modified matrix, while for the graphene composite the counterpart effect is load-dependent. The wearrate sensitivity to load is highest for the graphene composite in contact with steel, which indicates that the solid graphene film is stable only up to a certain limit of contact pressure. The balance between hardness (TiB₂) and lubricating effect (GNPs) is key to optimization – at higher loads, TiB₂ alone can be more effective against steel, while GNPs maintain the advantage in a ceramic friction pair.

3.7. Coefficient of friction

During the test of the rotational sliding motion against a ZrO₂ ceramic ball and a 100Cr6 steel ball, the coefficient of friction (COF) was recorded. The graphs in Fig. 6 show the COF during dry contact rotational sliding of the AlSi10Mg alloy and its two composite variants, AlSi10Mg-TiB₂ and AlSi10Mg-TiB₂--GNPs, using the "ball-on-disc" method. The measurements with the ZrO₂ ceramic ball and the 100Cr6 steel ball were compared at two normal loads of 0.25 and $0.5\,\mathrm{N}$. All measurements were taken over a $100\,\mathrm{m}$ track. The pure AlSi10Mg alloy has the highest initial COF at a load of 0.5 N and a 100Cr6 steel ball (Fig. 6d), but after the formation of a tribofilm, the COF gradually decreases. Although the addition of TiB₂ does not reduce the COF, it dramatically suppresses oscillations due to higher hardness and more uniform load transfer. The combination of TiB₂ + GNPs reduces friction compared to TiB₂, while maintaining good stability, indicating a synergistic effect of the lubricating graphene nanoplatelets and the TiB₂ supporting skeleton.

This phenomenon has also been observed in other hybrid composites based on aluminum, where hard ceramic particles (e.g., SiC) protect the soft matrix from plastic deformation, while graphene forms a low-shear tribofilm on the surface, which reduces adhesion and the resulting coefficient of friction [16]. At a load of 0.5 N and a $\rm ZrO_2$ ceramic ball (Fig. 6b), the $\rm ZrO_2$ ceramic ball causes higher adhesive components, and the composites show approximately 10 % more friction than the alloy alone. However, the reinforcements suppress fluctuations. At a half load of 0.25 N and a

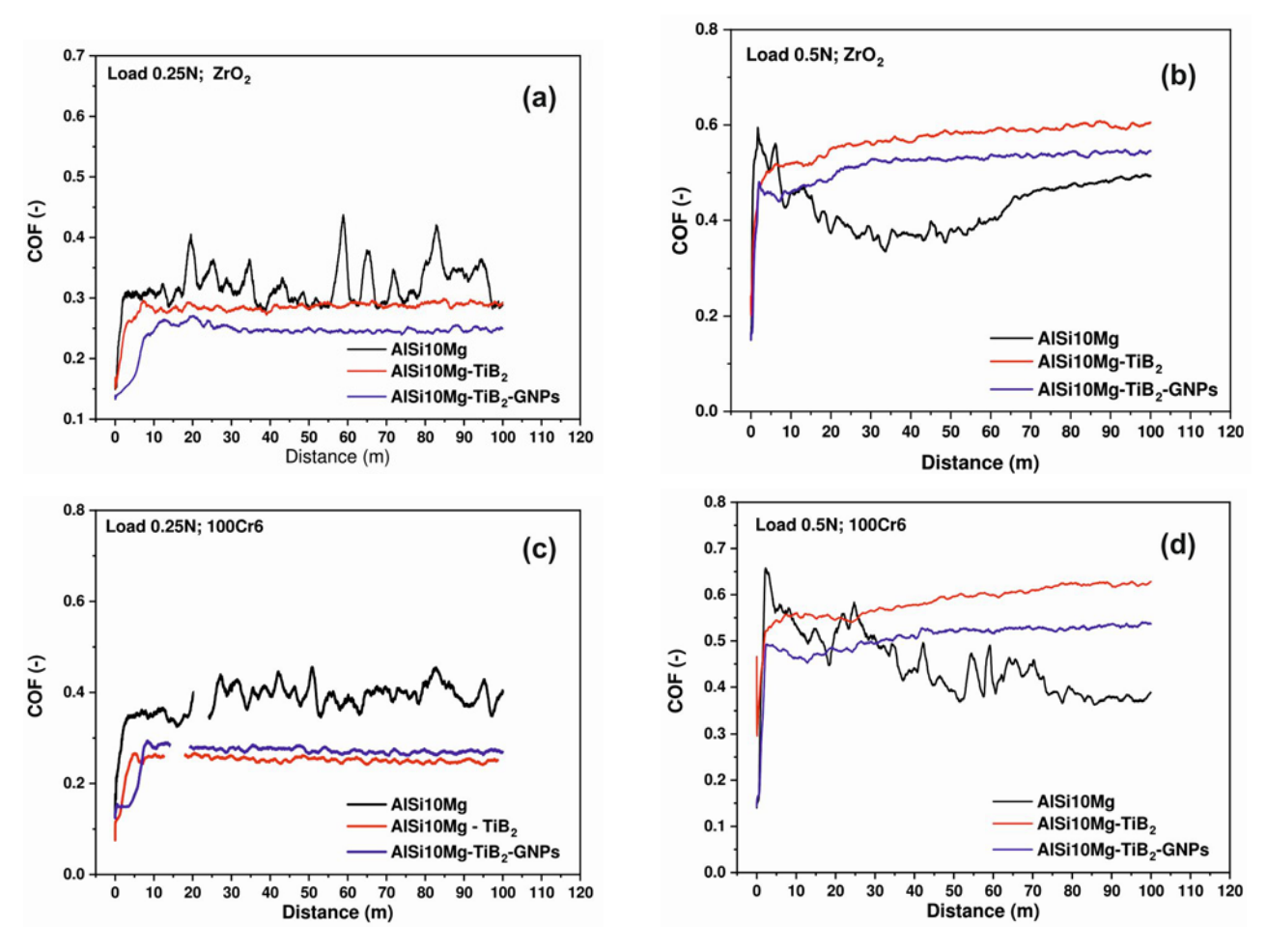


Fig. 6. Coefficient of friction (COF) for a ZrO₂ ceramic ball (a), (b) and a 100Cr6 steel ball (c), (d).

100Cr6 steel ball (Fig. 6c), the lubricating effect of the reinforcement is manifested; the composites reduce the COF by approximately 35 %. Graphene provides a slightly higher COF than TiB₂ alone, but still significantly below the value of the base alloy. At half load of 0.25 N and a ZrO₂ ceramic ball (Fig. 6a), the lubricating effect of the reinforcement was evident; the composites reduced the COF by approximately 20 %. For composites with ceramic particles, lower loading enhances the lubricating contribution of graphene (lowest COF). Peaks in the COF of the base alloy (stickslip) are suppressed in the composites. Increasing the load from 0.25 to $0.5\,\mathrm{N}$ raises the steady-state COF by $\sim 30\text{--}40\,\%$ for all materials. At higher loads, the overload of the contact surface dominates over the selflubricating effect of GNPs. Against a 100Cr6 steel ball, the base alloy achieves a lower final COF than against a ZrO₂ ceramic ball; the formation of a metallic transfer film on the steel probably reduces adhesion. The TiB₂ increases the microhardness of the matrix, thus limiting plastic deformation and peak retention. The result is smoother, but at higher loads, also a slightly higher COF due to the dominance of the abrasive component. The GNPs act as a solid lubricant, and at low pressure they are deposited in the tribofilm and reduce adhesion, but at high pressure the film is broken and the effect weakens, which is consistent with observations that the efficiency of the graphene layer decreases when the contact pressure exceeds its bearing capacity and it ruptures [17].

3.8. Wear mechanisms

The morphology and EDS maps of the worn track on a pure AlSi10Mg alloy after a rotational test against a ZrO₂ ceramic ball and a 100Cr6 steel ball are shown in Fig. 7. Parallel, approximately 5 to 20 µm wide lamellae of material oriented in the slip direction are formed along the entire width of the track. There are small gaps and cracks between the lamellae, and in places, peeled scales are visible. This "flow-type wear" is typical of intense plastic deformation of the soft AlSi10Mg matrix under the hard ZrO₂ ceramic ball (Fig. 7a). Sharp ridges are outlined in white. These are the kneaded sides of the plow grooves, where the material extruded by the cutting tips of the loosened particles by the plowing and micro-cutting mechanism has accumulated.

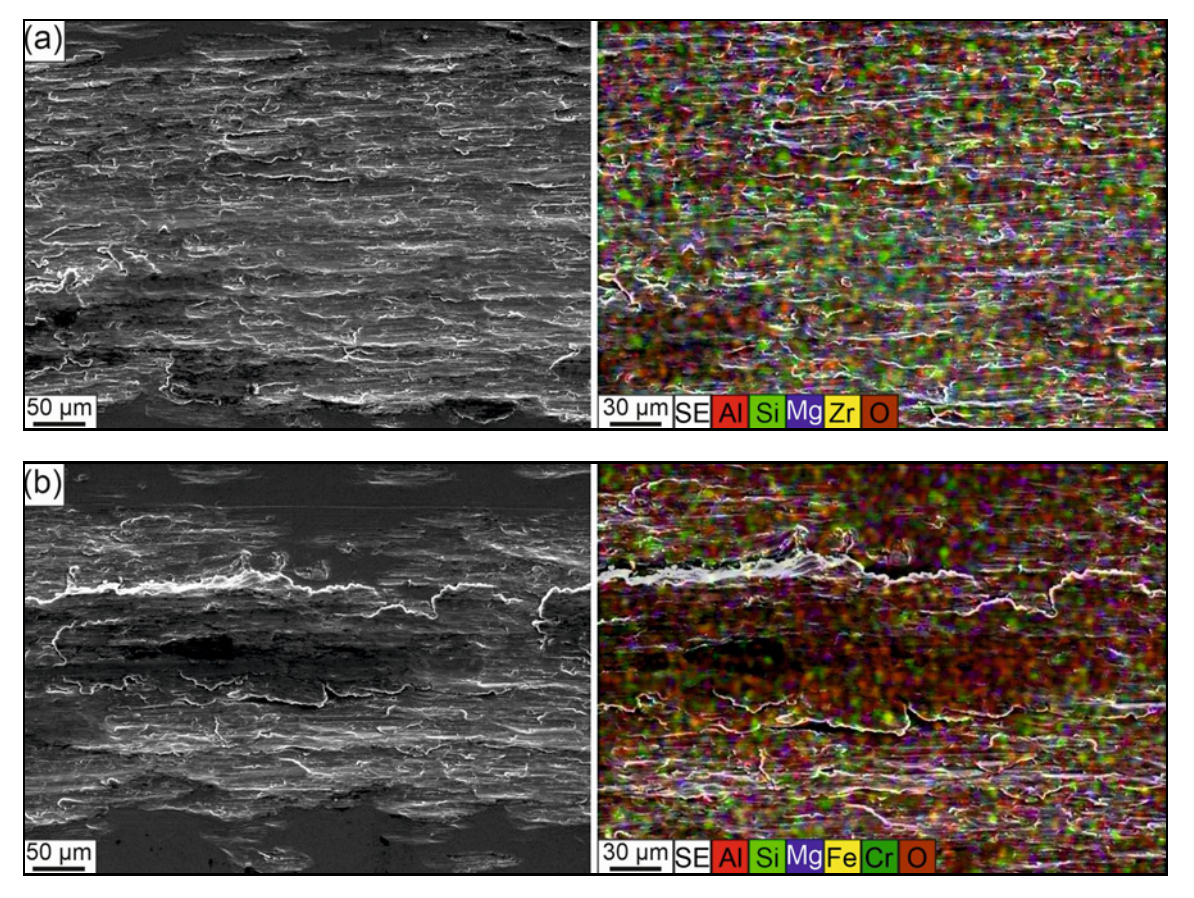


Fig. 7. SEM and EDS maps of wear marks on pure AlSi10Mg alloy after rotational slip testing against a ZrO₂ ceramic ball (a) and a 100Cr6 steel ball (b).

At the bottom of the image, a larger crater with exfoliated layers is visible, indicating that fatigue cracking below the surface has led to the tearing off of a fragment (local delamination – delamination wear). This mechanism is consistent with the classical delamination wear theory described by Suh [18]. The smoother surfaces between the lamellae have a gray texture without pores, indicating a continuous but thin oxide film that is continuously formed and subsequently stripped. The spatial distribution of elements in Fig. 7b indicates a combination of adhesive and abrasive wear. Both hard ZrO₂ and Si particles abrade the matrix, and simultaneously, the plastically deformed layers coalesce and exfoliate. The detected Zr confirms that the ball supplies additional abrasive particles, increasing friction and increasing the COF to approximately 0.50. The unstable oxide Al_2O_3/MgO tribofilm forms rapidly (due to the presence of oxygen on most of the surface), is discontinuous, and is periodically torn off, causing friction fluctuations and exposing fresh metal. The protruding eutectic Si phases worsen the "lubricating" effect of the oxide, as they protrude and act as micro-cutting components. The friction track of a pure AlSi10Mg alloy, after sliding against a ZrO₂ ceramic ball, exhibits strong plastic extrusion and lamellar shear bands. EDS reveals a mixed tribofilm of Al/Mg oxide with embedded ZrO₂ fragments and Si particles. Such behavior, where the soft aluminum matrix is intensively plastically deformed around the hard eutectic Si particles, is characteristic of sliding wear of Al-Si alloys [19].

The friction track of the pure AlSi10Mg alloy after sliding against a 100Cr6 steel ball (Fig. 7c) consists of extruded Al-matrix lamellae oriented parallel to the sliding direction, similar to the ZrO₂ ceramic ball. Less pronounced grooves are characteristic. In contrast to the contact with the ZrO₂ ceramic ball, deep plow grooves are almost absent with the 100Cr6 steel ball, which indicates the suppression of the purely abrasive component. EDS map analysis revealed a concurrent Fe-Cr-O overlay in a thick layer (Fig. 7d). This is a compact steel transfer from the ball, which was oxidized and mechanically mixed with Al oxide during the sliding process. In contrast to the ceramic counterpart, the steel locally welds to the aluminum matrix, detaches from the ball, and forms a mechanically mixed layer (MML) rich in Fe/Cr, which has a selflubricating effect. The steel film is harder than Al but softer than ZrO₂; it quickly smooths out during sliding and acts as a solid lubricant. This explains the lower average COF (~ 0.45) and smaller friction fluctuations compared to the test against ZrO₂. The high

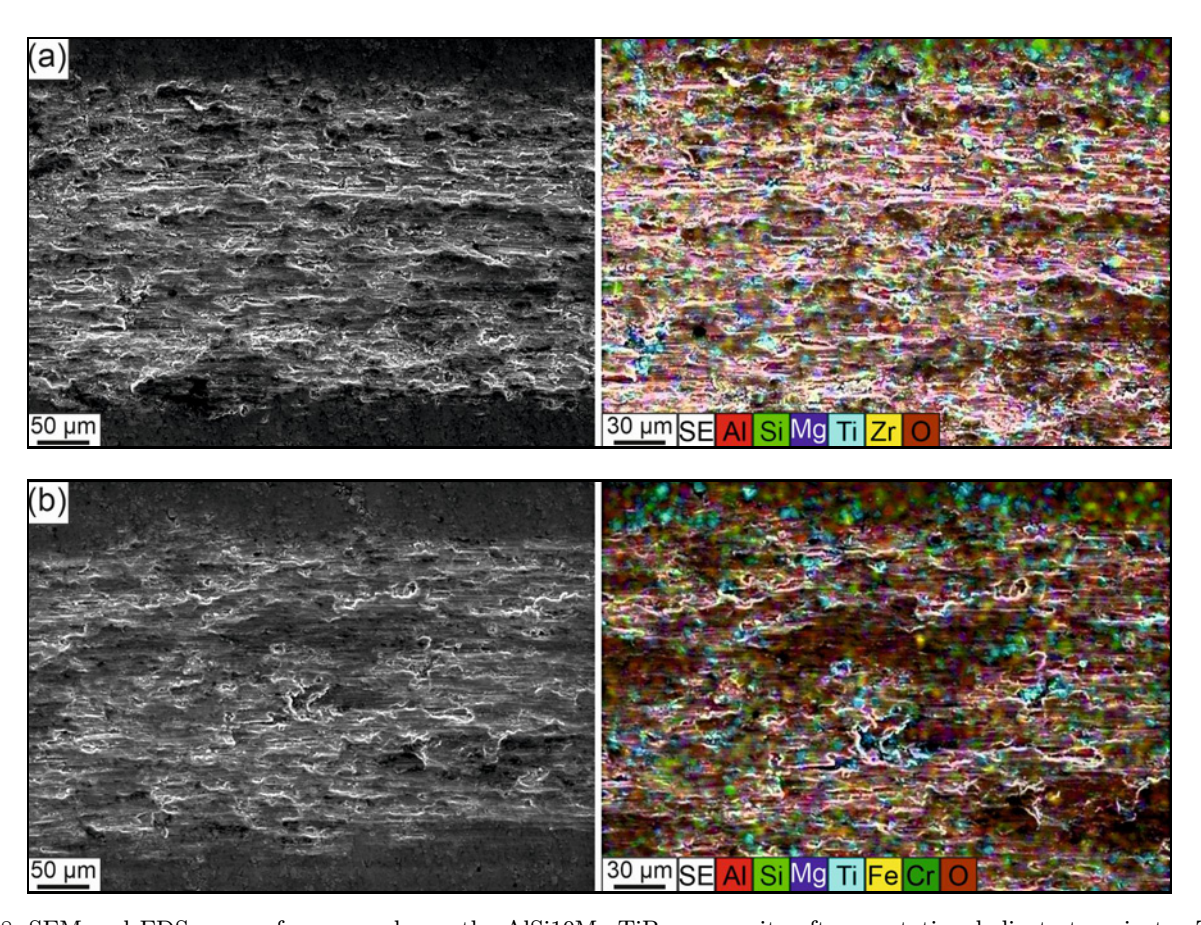


Fig. 8. SEM and EDS maps of wear marks on the AlSi10Mg-TiB $_2$ composite after a rotational slip test against a ZrO $_2$ ceramic ball (a) and a 100Cr6 steel ball (b).

O content together with Fe/Cr confirms the formation of tribochemical oxidation, which produces an oxide film and prevents direct metal-to-metal contact. The formation of a protective, iron-rich MML on the aluminum surface when sliding against steel is a key factor leading to friction stabilization and the transition from severe to moderate wear [20].

The surface of the AlSi10Mg-TiB₂ composite (Fig. 8a) is still lamellarly "deformed" in the direction of the yield, similar to that of pure AlSi10Mg, but the lamellae are narrower and less flattened than in the pure alloy. The hard TiB₂ particles dispersed in the matrix act as micro-beams that prevent large shear deformations, and the plastic flow is fragmented into shorter sections. This mechanism, where the hard particles carry part of the load and protect the soft matrix from extensive deformation, is a key benefit of ceramic reinforcement in metal matrix composites [21]. Darker, imperfect accumulations of fine dust (MML) are found between the lamellae. They are thicker precisely where the lamellae have ruptured. This involves the redeposition of loose fragments of Al-oxides, TiB₂, and ceramic debris from ZrO₂, resulting in the formation of so-called micro-islands within the tribofilm. Deep cavities and exfoliated scales, typical of a pure matrix, are almost absent; TiB₂ dissipates subsurface stresses and prevents the formation of long fatigue cracks (limited delamination). Although hard ZrO₂ particles still abrade the matrix, the presence of evenly distributed TiB₂ reduces the contact pressure on individual surface irregularities and thus also reduces the depth of the grooves. The Ti and O signals (Fig. 8b) strongly overlap, which indicates that the surface tribofilm is enriched with Ti-oxide/borate enamel formed from TiB₂. This enamel fills the microgrooves and acts as a solid lubricant. The hard, stiff TiB₂ particles increase the local hardness and elastic modulus, so that the Al matrix cannot "stretch" into wide lamellae; instead, narrow sections are formed, which are quickly covered by an oxide film. The tribochemical oxidation of $TiB_2 \rightarrow TiO_2/TiBO_x$ generates a very fine, low-shear coating. The tribochemical formation of a lubricating titanium dioxide (TiO₂) layer from TiB₂ particles during sliding wear is considered a significant factor contributing to the improvement of tribological properties [22]. Its presence, together with Al₂O₃/MgO, results in a lower and more stable COF (~ 0.27 –0.30) as recorded in the graph. The TiB₂ breaks long fatigue cracks into short, harmless segments, instead of exfoliating coarse scales. The surface is "crushed" into a thin powder layer that is recycled to the MML. Although ZrO₂ fragments are de-

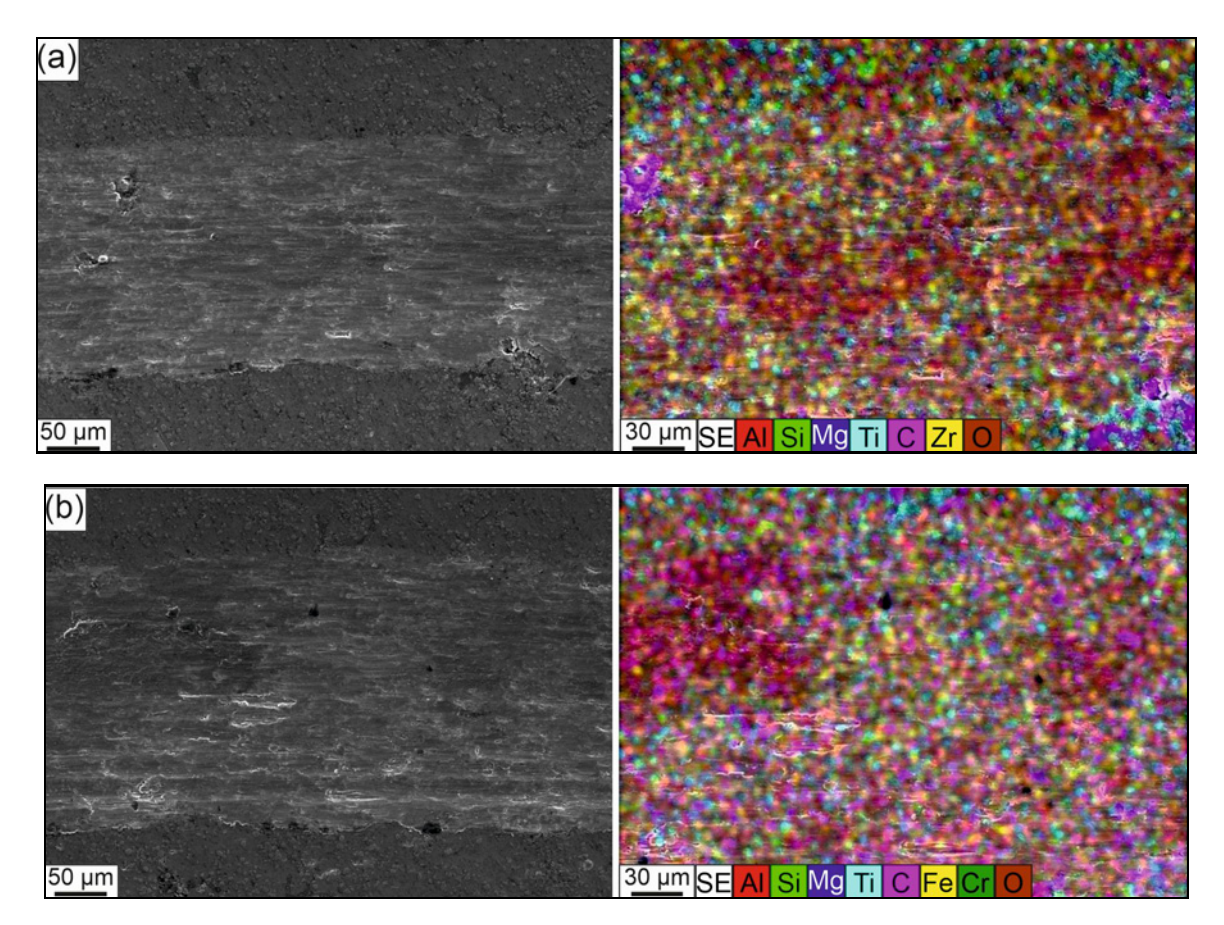


Fig. 9. SEM and EDS maps of wear marks on the AlSi10Mg-TiB₂-GNPs composite after a rotational slip test against a ZrO_2 ceramic ball (a) and a 100Cr6 steel ball (b).

tected, their erosive effect is weakened. The hard TiB₂ carries part of the load and creates an obstacle for the penetration of hard fragments deeper into the matrix.

The surface of the AlSi10Mg-TiB₂ composite after contact with a steel ball (Fig. 8c) consists of narrow lamellae oriented along the slip direction. Compared to the pure alloy, the lamellae are thinner and less flattened, which reflects the higher local hardness of the composite due to the dispersed TiB₂ reinforcement. In the central zone, there are darker, slightly embedded islands of the MML, which were formed by the deposition of fine Al-oxide dust, TiB₂ fragments, and steel transfer. The hard TiB₂ particles uniformly support the contact, thereby preventing deep plastic extrusion and delamination, which are typical of the unmodified matrix.

The Ti-O-Fe overlay (Fig. 8d) suggests the formation of a complex oxide glass (Al/Ti/Fe-oxides + borates), forming a compact film that fills microasperities and reduces shear stresses. Hard TiB₂ particles (HV $\sim 25\,\mathrm{GPa}$) carry a significant part of the normal force, thereby preventing local plastic flow of the AlSi10Mg matrix and reducing the depth of micro-cuts caused by Fe-rich fragments. The transferred Fe/Cr material from the ball mixes with oxidized Al and Ti, forming a compact tribofilm that acts

as a solid lubricant and dampens friction fluctuations (in the experiment, COF $\sim 0.24\text{--}0.26$ with negligible oscillations). TiB₂ blocks the propagation of subsurface fatigue cracks; instead of peeling off thick scales, only a thin powder layer is formed, which reintegrates into the MML. The formation of such a stable, protective, and multi-component mechanically mixed layer is the main cause of the transition to moderate wear and excellent tribological response [23].

The friction track on the AlSi10Mg-TiB₂-GNPs composite (Fig. 9a) is narrow; its microtopography consists of only very fine furrows in the direction of slip. Thick lamellae, deep plowing grooves, or caverns are clearly absent. Localized, isolated dark spots (pores/craters) are typically $\leq 10\,\mu\mathrm{m}$ in diameter; they were probably formed by the mechanical pulling out of TiB₂ grains or by pressing loose ZrO₂ fragments, which were subsequently covered by the coating. A continuous, low-contrast coating covers the edges of the track and its bottom. This is a nanolaminar graphene oxide film that smoothes out into a tribologically functional thin layer under slip.

The most marked feature is the continuous C signal (Fig. 9b), which follows the contours of the track, demonstrating that the graphene nanoplatelets have decomposed into a permanent tribo-carbon coating.

Its overlap with O and Ti indicates the formation of a C-TiO_x/Al₂O₃ type layer. The slip breaks and laminates the GNPs into several-nanometer plates, which overlap each other and form a low-shear film, resulting in a sharp drop in both adhesion and abrasive wear. This process of self-organization of graphene plates into a continuous, oriented layer with extremely low friction directly in the frictional contact is a well--documented phenomenon [24]. The hard TiB₂ particles will transfer a large part of the normal force, so that the graphene film does not deform plastically and remains continuous; this is the so-called "load bearing" effect of the TiB₂ particles. This synergistic interaction, where the hard ceramic phase carries the load and protects the lubricating graphene film from destruction, is the key mechanism responsible for the excellent tribological properties of the hybrid composites [25]. The tribochemical oxidation of Al/Mg/Ti in the presence of graphene yields a composite enamel (TiO₂-Al₂O₃-C-borate) that fills the microgrooves, binds loose particles, and stabilizes the film. The result is the lowest and most stable COF (~ 0.25) among all the materials investigated.

The friction track on the AlSi10Mg-TiB₂-GNPs composite, when tested against a steel ball (Fig. 9c), is $\sim 240 \,\mu\mathrm{m}$ wide, and its bottom is nearly planar. The microtopography consists of only fine grooves in the direction of slip. No deep grooves or cavities are visible. Several dark inclusions are visible, and shallow, white-rimmed islands indicate occasional pulling out of TiB₂ grains or re-deposition of the steel transfer, which was subsequently covered by a surface film. The homogeneous C signal (Fig. 9d) covering the entire track is evidence that the graphene nanoplatelets formed a continuous, self-lubricating film. The GNPs shear into nanometer-sized flakes during slip, which laminate each other and cover the steel transfer. The resulting film exhibits an extremely low slip coefficient, preventing direct Al-Fe adhesion. Although Fe/Cr fragments are released from the ball, they are quickly captured in the graphene oxide matrix - a MML without coarse ridges is formed, which dampens friction fluctuations. Hard particles (HV ~ 25 GPa) withstand peak pressures and prevent film damage. At the same time, they catalyze the formation of TiO₂/Ti-borates, which increase the film's wear resistance. The result is an extremely low and very stable COF of 0.23–0.25. The formation of a complex and stable tribofilm, which effectively immobilizes abrasive particles, is a characteristic feature of hybrid selflubricating composites [26].

4. Conclusions

1. AlSi10Mg-TiB₂ and AlSi10Mg-TiB₂-GNPs composite materials were successfully prepared by SPS.

The produced composites showed a microstructure with low porosity. Microstructural analysis of the AlSi10Mg-TiB₂ composite revealed that TiB₂ particles were successfully integrated into the matrix, primarily localized at the boundaries of the original powder particles. In the AlSi10Mg-TiB₂-GNPs hybrid composite, a tendency for graphene nanoplatelets (GNPs) to form agglomerates was observed; however, their addition still led to a significant improvement in tribological properties.

- 2. The base alloy AlSi10Mg showed low wear resistance, characterized by intense plastic deformation, delamination, and a high, unstable coefficient of friction ("stick-slip"). The wear mechanism was strongly dependent on the counterpart; against steel, a partially protective transfer film was formed, whereas against ceramics, abrasive and adhesive wear dominated.
- 3. The addition of TiB_2 particles led to a significant improvement in tribological properties. As a hard, supporting phase, TiB_2 prevented extensive plastic deformation of the matrix. During friction, TiB_2 tribochemically oxidized and formed a protective layer (glaze-film) rich in Ti-oxides, which contributed to the reduction and stabilization of friction.
- 4. The most significant progress was achieved with the hybrid composite, where a strong synergy between both types of reinforcement (${\rm TiB_2} + {\rm GNPs}$) was confirmed. The ${\rm TiB_2}$ particles served as a supporting skeleton, protecting the soft matrix and preventing mechanical destruction of the extremely slippery graphene film. The GNPs formed a continuous, self-lubricating film with low shear resistance on the surface, which drastically reduced adhesion and friction. The result of this synergy was an extremely smooth and stable tribofilm that effectively immobilized any abrasive particles, leading to the lowest and most stable coefficient of friction and a minimal wear rate among all the materials tested.
- 5. The conclusions clearly demonstrate that reinforcement hybridization, combining a hard support phase and a solid lubricant, is a highly effective strategy to overcome the tribological limitations of aluminum alloys and to develop advanced self-lubricating composites.
- 6. Recommended applications are, e.g., low-pressure sliding joints ($< 0.3\,\mathrm{N\,mm^{-2}}$) where the TiB₂ + GNPs composite can provide the lowest friction and high stability. For higher loads where stability and wear are a priority, the TiB₂ composite will provide the smoothest performance.

Acknowledgements

This work was supported by the Slovak National Grant Agency under the Project VEGA 2/0114/23.

References

- İ. Ovalı, C. Esen, S. Albayrak, H. Karakoç, M. S. Kumar, Ch.-H. Yang, Mechanical properties of Al2024/Al₂O₃/MgO/Graphite composites via hydrothermal hot pressing route, Mater. Chem. Phys. 302 (2023) 127779.
 - https://doi.org/10.1016/j.matchemphys.2023.127779
- [2] V. E. Ogbonna, P. Popoola, O. Popoola, Mechanical and tribological properties of nanoceramic reinforced aluminium-based nanocomposites for engineering applications, challenges and recommendations for future improvement: A review, J. Compos. Mater. 58 (2024) 3871–3914.

https://doi.org/10.1177/00219983241287758

- [3] F. Trevisan, F. Calignano, M. Lorusso, D. Manfredi, E. P. Ambrosio, On the selective laser melting (SLM) of the AlSi10Mg alloy: process, microstructure, and mechanical properties, Materials 10 (2017) 76. https://doi.org/10.3390/ma10010076
- [4] S. A. Sajjadi, H. R. Ezatpour, M. T. Parizi, Comparison of microstructure and mechanical properties of A356 aluminum alloy/Al₂O₃ composites fabricated by stir and compo-casting processes, Mater. Des. 34 (2012) 106–111.
 - https://doi.org/10.1016/j.matdes.2011.07.037
- [5] P. Bharathi, T. S. Kumar, Mechanical characteristics and wear behaviour of Al/SiC and Al/SiC/B₄C hybrid metal matrix composites fabricated through powder metallurgy route, Silicon 15 (2023) 4259–4275. https://doi.org/10.1007/s12633-023-02347-0
- [6] D. Berman, A. Erdemir, A. V. Sumant, Graphene: A new emerging lubricant, Mater. Today 17 (2014) 31– 42. https://doi.org/10.1016/j.mattod.2013.12.003
- [7] M. Tabandeh-Khorshid, E. Omrani, P. L. Menezes, P. K. Rohatgi, Tribological performance of selflubricating aluminum matrix nanocomposites: role of graphene nanoplatelets, Eng. Sci. Tech. Int. J. 19 (2016) 463–469.

https://doi.org/10.1016/j.jestch.2015.09.005

- [8] S. Basavarajappa, G. Chandramohan, K. Mukund, M. Aswin, M. Prabu, Dry sliding wear behavior of Al 2219/SiCp-Gr hybrid metal matrix composites, J. Mater. Eng. Perform. 15 (2006) 668-674. https://doi.org/10.1361/105994906X150803
- [9] W. Tian, S. Li, B. Wang, X. Chen, J.-H. Liu, M. Yu, Graphene-reinforced aluminum matrix composites prepared by spark plasma sintering, Int. J. Miner. Metall. Mater. 23 (2016) 723–729. https://doi.org/10.1007/s12613-016-1286-0
- [10] M. O. Durowoju, E. R. Sadiku, S. Diouf, M. B. Shongwe, I. M. Makena, M. M. Ramakokovhu, P. A. Olubambi, A. A. Eze, Wear and corrosion studies of graphite-aluminum composite reinforced with micro/nano-TiB₂ via spark plasma sintering, Mater. Wiss. Werkst. Tech. 50 (2019) 126–139. https://doi.org/10.1002/mawe.201700062
- [11] P. Shrivastava, S. N. Alam, T. Maity, K. Biswas, Effect of graphite nanoplatelets on spark plasma sintered and conventionally sintered aluminum-based nanocomposites developed by powder metallurgy, Mater. Sci.-Pol. 39 (2021) 346–370. https://doi.org/10.2478/msp-2021-0029

- [12] S. Arunkumar, M. S. Sundaram, K. M. S. Kanna, S. Vigneshwara, A review on aluminium matrix composite with various reinforcement particles and their behavior, Mater. Today Proc. 33 (2020) 484–490. https://doi.org/10.1016/j.matpr.2020.05.053
- [13] N. T. Aboulkhair, I. Maskery, C. Tuck, I. Ashcroft, N. M. Everitt, The microstructure and mechanical properties of selectively laser melted AlSi10Mg: the effect of a conventional T6-like heat treatment, Mater. Sci. Eng. A 667 (2016) 139–146. https://doi.org/10.1016/j.msea.2016.04.092
- [14] M. Hadian, H. Shahrajabian, M. Rafiei, Mechanical properties and microstructure of Al/(TiC+TiB₂) composite fabricated by spark plasma sintering, Ceram. Int. 45 (2019) 12088–12092. https://doi.org/10.1016/j.ceramint.2019.03.106
- [15] N. Seyed Pourmand, H. Asgharzadeh, Aluminum matrix composites reinforced with graphene: a review on production, microstructure, and properties, Crit. Rev. Solid State Mater. Sci. 45 (2020) 289–337. https://doi.org/10.1080/10408436.2019.1632792
- [16] A. Nirala, S. Soren, N. Kumar, M. A. Khan, S. Islam, N. K. Khan, Micro-mechanical and tribological behavior of Al/SiC/B₄C/CNT hybrid nanocomposite, Sci. Rep. 13 (2023) 13147. https://doi.org/10.1038/s41598-023-39713-2
- [17] L. Wu, Z. Zhao, P. Bai, W. Zhao, Y. Li, M. Liang, H. Liao, P. Huo, J. Li, Wear resistance of graphene nanoplatelets (GNPs) reinforced AlSi10Mg matrix composite prepared by SLM, Appl. Surf. Sci. 503 (2020) 144156. https://doi.org/10.1016/j.apsusc.2019.144156
- [18] N. P. Suh, The delamination theory of wear, Wear 25 (1973) 111–124. https://doi.org/10.1016/0043-1648(73)90125-7
- [19] H. Goto, K. Uchijo, Wear mechanism of Al–Si alloy impregnated graphite composite under dry sliding, Wear 259 (2005) 613–619. https://doi.org/10.1016/j.wear.2005.02.024
- [20] P. H. Shipway, A. R. Kennedy, A. J. Wilkes, Sliding wear behaviour of aluminium-based metal matrix composites produced by a novel liquid route, Wear 216 (1998) 160–171. https://doi.org/10.1016/S0043-1648(97)00153-1
- [21] R. L. Deuis, C. Subramanian, J. M. Yellup, Dry sliding wear of aluminium composites—a review, Compos. Sci. Technol. 57 (1997) 415–435. https://doi.org/10.1016/S0266-3538(96)00167-4
- [22] N. B. Dhokey, K. K. Rane, Wear behavior and its correlation with mechanical properties of TiB₂ reinforced aluminium-based composites, Adv. Tribol. 2011 (2011) 837469. https://doi.org/10.1155/2011/837469
- [23] M. Nosonovsky, P. K. Rohatgi, Tribological properties of metal matrix composites, In: Biomimetics in Materials Science, Springer, New York (2011) 241–267. https://doi.org/10.1007/978-1-4614-0926-7-8
- [24] R. Buzio, A. Gerbi, C. Bernini, L. Repetto, A. Vanossi, Graphite superlubricity enabled by triboinduced nanocontacts, Carbon 184 (2021) 875–890. https://doi.org/10.1016/j.carbon.2021.08.071
- [25] F. Lin, J. Wang, H. Wu, F. Jia, Y. Lu, M. Ren, M. Yang, Z. Chen, Z. Jiang, Synergistic effects of TiC and graphene on the microstructure and

tribological properties of Al2024 matrix composites, Adv. Powder Technol. 32 (2021) 3635–3649. $\underline{\text{https://doi.org/10.1016/j.apt.2021.08.015}}$ [26] P. Ravindran, K. Manisekar, R. Narayanasamy, P. Narayanasamy, Tribological behaviour of powder metallurgy-processed aluminium hybrid composites with the addition of graphite solid lubricant, Ceram. Int. 39 (2013) 1169–1182.

https://doi.org/10.1016/j.ceramint.2012.07.041